

Article

Multi-Mode Vector Light Field Generation Using Modified Off-Axis Interferometric Holography and Liquid Crystal Spatial Light Modulators

Wenxu Zhu ¹, Feilong Gao ¹, Qianqian Fu ¹, Xinlong Zhou ¹, Yiyang Xie ^{1,*}, Bingyuan Zhang ^{1,*} and Santosh Kumar ^{1,2}

¹ Shandong Key Laboratory of Optical Communication Science and Technology, School of Physics Science and Information Technology, Liaocheng University, Liaocheng 252059, China; santosh@lcu.edu.cn (S.K.)

² Department of Electronics and Communication Engineering, K L Deemed to be University, Guntur 522302, Andhra Pradesh, India

* Correspondence: xieyiyang@lcu.edu.cn (Y.X.); zhangbingyuan@lcu.edu.cn (B.Z.)

Abstract: The increasing enhancement in the modulation accuracy of spatial light modulators has garnered significant attention towards real-time control technology for light fields based on these modulators. It has been demonstrated that this technology possesses a remarkable capability to generate vector beams with arbitrary complex amplitude distributions. Nevertheless, past studies indicate that the generation of only one vector beam at a time has been observed. The simultaneous generation of numerous vector light fields can give rise to several challenges, including compromised picture quality, limited single-mode operation, and intricate optical path configurations. In pursuit of this objective, we present a novel methodology that integrates the coding methodology of modified off-axis interferometric holography with the idea of optical superposition. This technique facilitates the concurrent generation of several vector beams. In this study, we present a demonstration of the simultaneous creation of twelve vector beams using a single spatial light modulator (SLM) as a proof of concept. Significantly, this technology has the ability to generate an unlimited quantity of vector light fields concurrently under the assumption that the resolution of the SLM does not impose any limitations. The findings indicate that the imaging quality achieved by this technology is of a high standard. Furthermore, it is possible to separately control the beam waist radius, topological charge, polarization order, and extra phase of each beam.

Keywords: spatial light modulator; modified off-axis interferometric hologram; multimode vector light field



Citation: Zhu, W.; Gao, F.; Fu, Q.; Zhou, X.; Xie, Y.; Zhang, B.; Kumar, S. Multi-Mode Vector Light Field Generation Using Modified Off-Axis Interferometric Holography and Liquid Crystal Spatial Light Modulators. *Photonics* **2024**, *11*, 33. <https://doi.org/10.3390/photonics11010033>

Received: 5 December 2023

Revised: 22 December 2023

Accepted: 26 December 2023

Published: 29 December 2023



Copyright: © 2023 by the authors. Licensee MDPI, Basel, Switzerland. This article is an open access article distributed under the terms and conditions of the Creative Commons Attribution (CC BY) license (<https://creativecommons.org/licenses/by/4.0/>).

1. Introduction

Presently, nearly all applications involving light rely on the dimensional resources of photons. It is common knowledge that electrons possess extremely restricted dimensions, such as electron spin. Photons, on the other hand, are distinguished by multiple dimensions. Photons' fundamental dimensions consist of wavelength/frequency, time, complex amplitude, polarization, and spatial domain. By modifying the photons' spatial domains, one can generate a vector light field. The polarization characteristics of the vector field cause it to have broad application prospects in the fields of transverse or longitudinal super-resolution [1,2], optical needle [3,4], optical information transmission [5], optical chain [6], optical channel [7], particle capture, and manipulation [8,9].

Obviously, the generation of a vector light field is the premise of studying its novel characteristics and developing new applications for it. In previous reports, the known generation techniques were mainly divided into the intracavity method and the extracavity method. The intracavity method requires the addition of a specific polarized optical element [10–12] or a grating element [13] to generate a specific vector light field, and if a

new vector field is to be generated, a new harmonic oscillation cavity must be designed and installed. Therefore, the method is greatly discounted for the real-time regulation of the light field. In contrast, the extra-cavity method is very flexible. Different vector light fields can be obtained by adjusting the optical path or element, which makes the generation of vector light fields diverse. The main devices involved are the optical metasurface [14,15], q plate [16], cylindrical lens [17,18], bifurcated grating [19], spiral phase plate [20,21], and SLM [22]. Among them, the polarization state and complex amplitude distribution of the vector light field can be adjusted in real time by means of an SLM, which highlights the flexibility of the extra-cavity method. Therefore, the vector light field generation method based on an SLM is widely used. For example, Ding's research group [23] divided the incident beam into two beams from a computer-generated hologram (CGH) written to the SLM. Each beam is encoded using the specified complex field, and then effectively combined into a single vector beam through the Wollaston prism. In the triangular copass interferometer system proposed by Zhao Jianlin's research group [24], a beam of light passes through the beam splitting system first, and then two orthogonal polarization components are reflected by a right-angle prism to the left and right regions on the screen of the SLM, respectively, and then coupled through the combined beam system to form a single vector beam. Carmelo et al. [25] could simultaneously generate multiple vector beams with different spatial shapes and polarization distributions by using the interference method and the optical superposition principle. Compared with the former two, this greatly improves the generation efficiency of vector beams and increases the types of generation. However, it is limited to the generation of vector beams with cylindrical symmetry. In the path, it is necessary to use wave plates to make adjustments, and the requirements for optical path construction are strict, which will increase the difficulty of the actual operation.

In this paper, a modulation method based on a liquid crystal SLM is proposed. By using the coding method based on the modified off-axis interference hologram, combined with the transmission liquid crystal SLM and a shunt coupling system, the multimode vector light field with an arbitrary complex amplitude distribution is finally generated. Complex optical components are not involved in the whole experiment. The optical system is small in size, which reduces the complexity of the experimental optical path, and the vector beam quality is high. As a proof of principle, the experimental results not only show that this method can generate multiple types of vector beams at the same time, but also that the beam waist radius, topological charge number, polarization order, and additional phase of each beam are independently controllable. In addition, although we only show 12 cylindrically symmetric vector beams, the actual number is much larger than this, which is mainly limited by the resolution of the SLM. If the resolution region of the SLM is idealized, infinite vector beams can be generated. Section 2 introduces the experimental methods and theoretical analysis of this work. Section 3 shows the experimental results and discussion.

2. Materials and Methods

2.1. Experimental Device and Method

Figure 1a is the schematic diagram of the experimental system proposed using this method. Based on the principle of interference fringe recording of optical holography and digital holography, this method uses the Matlab platform and combines the modified off-axis interference coding method to make the computer-generated hologram. During the encoding, the complex amplitude obtained by each sampling point on the hologram is converted into the hologram transmittance, and the gray-scale CGH is generated. The required CGH is displayed on the SLM, where the SLM is equivalent to a two-dimensional diffraction grating, which is used to assign a specific carrier frequency to the diffracted beams at all levels. The pixel size of the SLM is 1024×768 , and the pixel size is $18 \mu\text{m}$. A collimated beam of light with a wavelength of 632.8 nm is modulated by a SLM and divided into multi-level diffraction beams, which are then spatially transformed by a Fourier lens L_1 . The corresponding spectral points will appear on the back focal plane of L_1 . In order to

prevent the generation of unnecessary noise, a double-channel pinhole filter (PF, as shown in Figure 1b) is placed here, allowing only the required level 1 diffraction through which the other levels of diffraction are blocked; the diffraction angle diagram between the first-order diffraction order and the zero-order diffraction order is shown in Figure 1c, and the angle is α . Subsequently, the two beams of diffraction light are separated by the triangular reflective prism, R_r , through which one beam of diffusion light reaches the polarization beam splitter (PBS) through the reflective M_1 , and its polarization is modulated to the horizontal state, during which time two reflections (R_r and M_1) are experienced. The other beam of diffraction light passes through the M_2 reflector, M_3 passes to the PBS, and its polarization state is adjusted to a vertical, during which time 4 reflections are experienced (R_r , M_2 , M_3 , and PBS), because both beams have experienced even-numbered reflections, so the original light field in the PBS can be combined. In this method, the carrier frequency in the z direction is increased to accurately control the optical path difference when encoding and calculating the hologram, so that the optical path of the two diffracted beams is the same. Finally, the two beams are coupled at PBS to generate the required vector light field, which is imaged on the charge-coupled device (CCD) by the Fourier lens L_2 and recorded. The pixel size of the CCD is 6000×4000 , and the resolution is 72 dpi. The experimental results can be used to analyze the polarization state by placing a polarizer in front of the CCD.

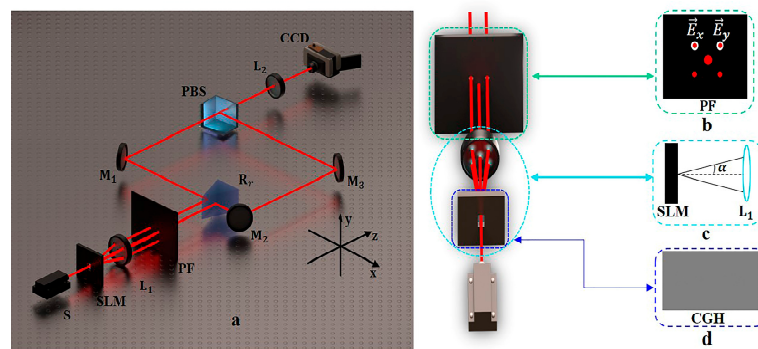


Figure 1. The schematic diagram and local section structure diagram of the experimental device. (a) S: He-Ne light source; SLM: transmission liquid crystal spatial light modulator; L_1 – L_2 : lens; PF: dual-channel pinhole filter; R_r : triangular reflection prism; M_1 , M_2 , M_3 : mirrors; PBS: polarization beam splitter; CCD: charge-coupled device. (b) The schematic diagram of the dual-channel pinhole filter and the spatial spectrum diagram of the L_1 back focal plane of the lens. (c) Diffraction angle chart between first-order and zero-order diffraction levels. (d) CGH loaded on the SLM.

2.2. Principle Analysis

As an electromagnetic wave, any electric field vector perpendicular to the propagation direction z can be decomposed into two orthogonal vectors in the x and y directions. Therefore, the polarization state of light or the electric field vector can be expressed by the vector sum of these two orthogonal components [26]:

$$\vec{E} = \begin{bmatrix} U_x(x, y) \\ U_y(x, y) \end{bmatrix} = \begin{bmatrix} E_x \exp(j\varphi_x) \\ E_y \exp(j\varphi_y) \end{bmatrix} \quad (1)$$

Among them, (U_x, U_y) is the complex amplitude of the two polarization components, (E_x, E_y) and (φ_x, φ_y) are the amplitude and phase distribution of the two polarization components, and j is the imaginary symbol.

On the input plane, it is assumed that the complex amplitude transmittance function $T(x, y)$ loaded on the SLM can be expressed as the following matrix form:

$$T(x, y) = \begin{bmatrix} t_{11} & t_{12} & t_{13} & \dots & t_{1b} \\ t_{21} & t_{22} & t_{23} & \dots & t_{2b} \\ \vdots & \ddots & \ddots & \ddots & \vdots \\ t_{a1} & \dots & \dots & \dots & t_{ab} \end{bmatrix} \quad (2)$$

where a represents the number of rows in the matrix, and b represents the number of columns in the matrix.

In order to make full use of the gray level and pixel resolution of the SLM, taking the commonly used modified off-axis interferometric CGH as an example, the CGH in this method can be encoded according to the following formula:

$$t(x, y) = \beta |1 + U_x(x, y) \exp[jk_\alpha(x + y + z_x)]|^2 + \beta |1 + U_y(x, y) \exp[jk_\alpha(-x + y + z_y)]|^2 \quad (3)$$

Here, the constant β represents the loss coefficient of the beam after passing through the liquid crystal spatial light modulator, with a value range of $[0, 1]$, which can be ignored in coding; α is the diffraction angle between the first-order diffracted light and the zero-order diffracted light; $k_\alpha = 2\pi \sin \alpha / \lambda$ is the spatial carrier frequency, and λ is the wavelength of the input light; and $\exp[jk_\alpha(x + y + z_x)]$ and $\exp[jk_\alpha(-x + y + z_y)]$ are the carrier frequency components of U_x and U_y on the x , y , and z axes, respectively, where z is the constant introduced by adjusting the optical path of two diffracted beams and can be ignored after adjusting the optical path of the two diffracted beams to be equal in the later period. The negative sign only indicates that U_x and U_y are encoded in the diffraction directions of $+45^\circ$ and -45° , respectively, with the x axis, which is convenient for spatial filtering in the later period.

Assuming that the incident plane light field is \vec{E}_{in} , the output light field after the action of the CGH can be expressed as

$$\vec{E}_{out}(x, y) = \vec{E}_{in} T(x, y) \quad (4)$$

where \vec{E}_{in} is the complex amplitude of the input light field, and \vec{E}_{out} is the complex amplitude of the output light field.

For ease of explanation, proceed with the interference only when $a = b = 1$, in which case, the transmission function of the hologram can be calculated, $T_{11}(x, y) = t(x, y)$, and it can be replaced with the following formula:

$$\vec{E}_{out}(x, y) = \vec{E}_{in} T_{11}(x, y) = \beta \vec{E}_{in} \left\{ \begin{array}{l} E_0 + U_x(x, y) \exp[jk_\alpha(x + y + z_x)] \\ + U_x^*(x, y) \exp[-jk_\alpha(x + y + z_x)] \\ + U_y(x, y) \exp[jk_\alpha(-x + y + z_y)] \\ + U_y^*(x, y) \exp[-jk_\alpha(-x + y + z_y)] \end{array} \right\} \quad (5)$$

Here, E_0 represents the amplitude of the incident light, and “*” represents the complex conjugate operation. It is clear that the second and fourth elements of the $\{ \}$ are necessary for the vector light field through the dual-channel pinhole filter for space filtration, only the required part can pass, and using the triangular reflective prism splitting, components can be obtained for the final generation of the two beam light field components, whose complex amplitude distribution is as follows:

$$\vec{E}_x^{11}(x, y) = \beta \vec{E}_{in} U_x(x, y) \exp[jk_\alpha(x + y + z_x)] \quad (6)$$

$$\vec{E}_y^{11}(x, y) = \beta \vec{E}_{in} U_y(x, y) \exp[jk_\alpha(-x + y + z_y)]$$

The above formula shows that there is a surplus of phase factors after the required U_x and U_y due to the impact of the time load frequency of the encoding hologram. In order to eliminate this influence, it is possible to adjust the light path so that the two beams of diffuse light spread along the z axis; at this time, $x = y = 0$. At the same time, when the beams are equal in the diffused light range, $\exp(jk_x z_x) = \exp(jk_y z_y)$. Therefore, the above formula can be simplified as follows:

$$\vec{E}_x^{\rightarrow 11}(x, y) = \beta \vec{E}_{in} U_x(x, y), \vec{E}_y^{\rightarrow 11}(x, y) = \beta \vec{E}_{in} U_y(x, y) \quad (7)$$

The Jones matrix of the two incident surfaces at the PBS can be expressed in the following form:

$$J_{PBS_0} = \begin{bmatrix} 1 \\ 0 \end{bmatrix}, J_{PBS_e} = \begin{bmatrix} 0 \\ 1 \end{bmatrix} \quad (8)$$

Since the two polarization components need to be coupled by a polarization splitting prism, the final output vector light field can be expressed as

$$\vec{E}_{out}^{\rightarrow 11} = \vec{E}_x^{\rightarrow 11}(x, y) J_{PBS_0} + \vec{E}_y^{\rightarrow 11}(x, y) J_{PBS_e} = \beta \vec{E}_{in} \begin{bmatrix} U_x(x, y) \\ U_y(x, y) \end{bmatrix} = \beta \vec{E}_{in} \vec{E}_{11} \quad (9)$$

Similarly, if a and b take any values,

$$\vec{E}_{out}^{\rightarrow ab} = \beta \vec{E}_{in} \begin{bmatrix} E_{11} & E_{12} & E_{13} & \dots & E_{1b} \\ E_{21} & E_{22} & E_{23} & \dots & E_{2b} \\ \vdots & \ddots & \ddots & \ddots & \vdots \\ E_{a1} & \dots & \dots & \dots & E_{ab} \end{bmatrix} \quad (10)$$

Therefore, through the coding method and optical path construction of the above design, the required multi-mode vector light field can be obtained in the recording plane.

3. Results and Discussion

In order to ensure that the two orthogonal polarization components have independent imaging capabilities and to determine the system parameters, two binary grayscale images with black and white in Figure 2a,b are substituted into Equation (2) as the U_x component and the U_y component, respectively, to control the additional phase of the vector light field. The period and distribution of the moiré fringes (as shown in Figure 2c) generated during the control process can explain the periodic difference between the two orthogonal polarization components and the direction of relative tilt. The system parameters can be defined by eliminating the moiré fringes (as shown in Figure 2d), which is known by calculating Formula (1), where controlling a vector beam requires the modulation of its four degrees of freedom, respectively; that is, the two vertical partitions of a vector beam will have their respective spatial frequency parameters k_x in the x and y directions, and by modulating the four spatially frequency partition parameters separately, the U_x component and U_y component are finally common and coplanar.

The background gray values in Figure 2a,b are 1 and 0, respectively, and the gray values of 'O', 'P', 'T', 'I', 'C', and 'S' are 0 and 1, respectively. The additional phases corresponding to the image gray values of 0 and 1 are 0 and $\pi/2$, respectively. Figure 2d shows that the intensity of the light field is evenly distributed without the polarizer, because the amplitude of the light field is not additionally regulated. When the polarization direction of the polarizer is horizontal, the light intensity of the background light is the smallest, and the light intensity of the four characters of 'O', 'P', 'T', 'I', 'C', and 'S' of horizontal linear polarization is the largest. The experimental results are shown in Figure 2e. When the polarization direction of the polarizer is 45° , the light intensity of the characters 'O', 'P', 'T', 'I', 'C', and 'S' is the same as that of the background light. The experimental results are shown in Figure 2f. When the polarization direction of the polarizer is vertical, the

light intensity of the background light is the largest, and the light intensity of the four characters of 'O', 'P', 'T', 'I', 'C', and 'S' is the smallest. The experimental results are shown in Figure 2g. When the polarization direction of the polarizer is 135°, the intensity of the four characters of 'O', 'P', 'T', 'I', 'C', and 'S' is the same as that of the background light. The experimental results are shown in Figure 2h. Through the above experimental results, it can be seen that in the case of a polarizer, due to the background and the different polarization directions of different words, different light intensity distribution effects will be presented. It is verified that the two orthogonal polarization components of the vector beam in this method have good imaging abilities, and the additional phase is controllable.

In order to verify that this method can produce multiple vector light fields simultaneously, a special calculated holography is produced. The first row of the figure, from left to right, shows the diameter of the vector beam and the rotating vectorial beam of light, and the second row shows the vibrant beam, as shown in Figure 3a.

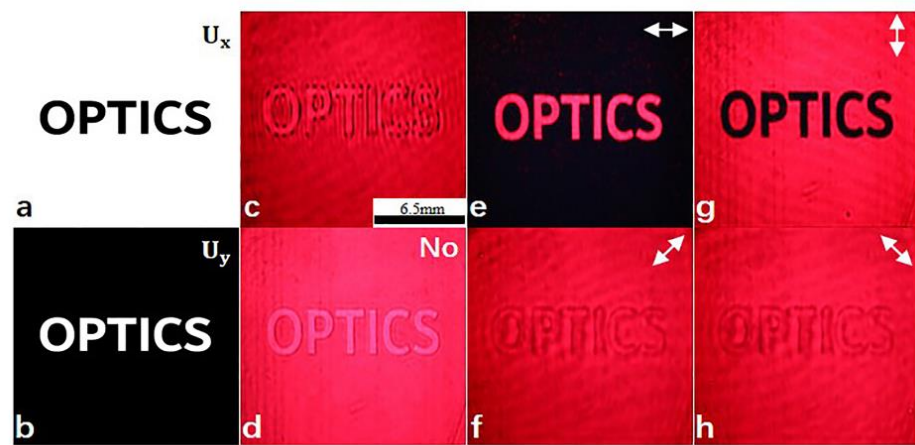


Figure 2. (a,b) Black and white binary grayscale; (c) the light intensity distribution with Moiré fringes; (d) the light intensity distribution after eliminating the Moiré fringes and without the polarizer; (e–h) the light field intensity distribution of the polarizer at 0°, 45°, 90°, and 135°.

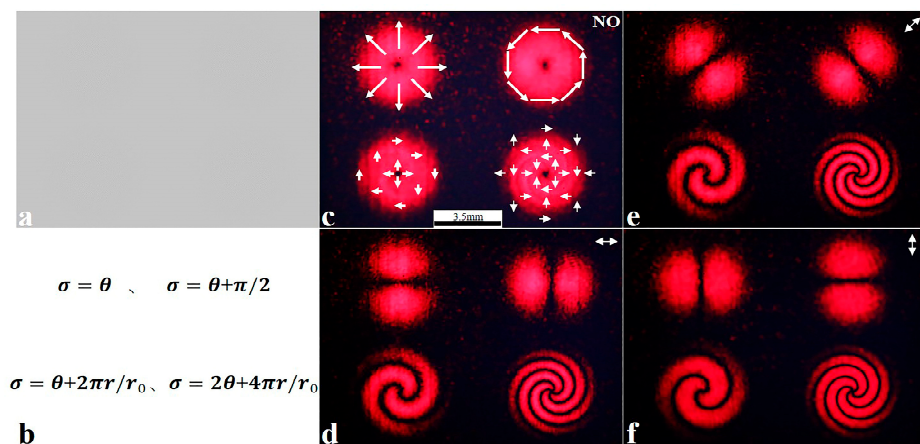


Figure 3. (a) Specially designed two-row two-column computational hologram; (b) the specific parameters corresponding to each beam; (c) the light field intensity distribution without polarizer; (d–f) the light field intensity distribution of the polarizer at 0°, 45°, and 90°.

The additional phase of the column-symmetric vector light field can be synthesized with the rotating variable and the diameter variable in both cases, so its additional phase can be expressed as

$$\sigma = m\theta + 2n\pi \frac{r}{r_0} + \varphi_0 \tag{11}$$

Among them, (r, θ) is the polar coordinate of the input plane, satisfying $r = \sqrt{x^2 + y^2}$, $\theta = \tan^{-1}(y/x)$, where r is the radius on the cross section of the light wave, r_0 is the spot radius of the Hermitian Gaussian beam, φ_0 is the initial phase, integer m is the topological charge of the required vector beam, and n is the radial index of the required vector beam.

Figure 3c shows the light field intensity distribution map without the polarizer, and the polarization direction of each point is marked in the map. Figure 3d–f show the intensity distribution of the light field when the polarizer is at 0° , 45° , and 90° , respectively. It can be seen from these three subfigures that when the angle of the polarizer changes, the radial vector beam and the azimuth vector beam will change accordingly. In this process, the extinction direction of the radial vector beam is always perpendicular to the polarizer, while the azimuth vector beam rotates counterclockwise at the same angle. In summary, this method can produce multiple vector light fields at the same time and improve image quality.

In order to ultimately determine that this method can produce several different types of vector beams simultaneously and that each beam can be independently controlled by its waist radius, topological charge number, polarization order, and additional phase, a special design of a multi-vector light field holography shows a total of 12 different patterns (take $a = 3, b = 4$): the first row shows four kinds of Laguerre-Gaussian vector light beams, and vector beams with different radial exponents and topological charges are shown in the second and third rows, as seen in Figure 4a.

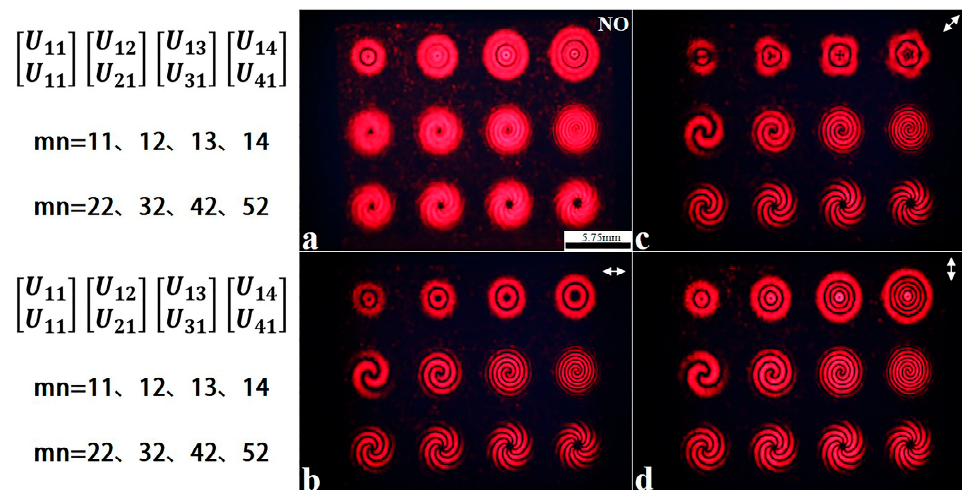


Figure 4. (a) The light field intensity distribution without polarizer; (b–d) the light field intensity distribution of the polarizer at 0° , 45° , and 90° .

Among them, the Laguerre-Gaussian beam, a typical spiral phase distribution of uneven turbulent vector beams, can be rewritten (1) as

$$\vec{E} = \begin{bmatrix} U_x(x, y) \\ U_y(x, y) \end{bmatrix} = \begin{bmatrix} U_{n_1 m_1}(x, y) \\ U_{n_2 m_2}(x, y) \end{bmatrix} \quad (12)$$

Among them,

$$U_{mn}(x, y) = C_{mn} \left(\frac{\sqrt{2}}{\omega_0} \right)^{|m|} L_n^m \left(\frac{2r^2}{\omega_0^2} \right) \exp \left(im\varphi - \frac{r^2}{\omega_0^2} \right) \quad (13)$$

where C_{mn} is the normalized constant, ω_0 is the beam width, and L_n^m is the Laguerre polynomial. A scalar Laguerre-Gaussian beam is a typical optical vortex whose topological charge is equal to an integer, m . For Laguerre-Gaussian vector beams, due to the existence of the orthogonal polarization state, the topological charge has different vectors.

The results shown in Figure 4a–d are the experimental results of a multimode vector light field without a polarizer at 0° , 45° , and 90° , respectively.

Figure 4a shows the sampling of the total intensity distribution of the output multimode vector beam by CCD when the polarizer is not placed. Due to the lack of additional regulation of the complex amplitude of the light field, the light intensity of each spot is evenly distributed in this state. There are central dark spots in the 12 patterns in the figure. The central dark spot in the first row is caused by the fact that the center of the Laguerre-Gaussian beam is a dark core, that is, the central light intensity here is zero. In the second row, when the topological charge m is constant, the area of the central dark spot will decrease with the increase in the radial index n . In the third row, when the radial index n is constant, the area of the central dark point will increase with the increase in the topological load m . The central dark point in the second row and the third row is collectively referred to as the phase singularity. The reason for the phase singularity is that the phase of the light wave field becomes uncertain, and the amplitude of the field is zero. Another reason is that the polarization distribution of the polarized light at the center point is the same, but the phase is the opposite, so the interference condition is satisfied, and the destructive interference dark spot is formed. Figure 4b shows the intensity distribution of the multimode vector beam when the polarizer is 0° . It can be seen from the diagram that when the first row n is constant, the radius of the extinction ring increases gradually with the increase in the topological charge m . The second row, with the increase in the radial index n , the radius of the spiral extinction gradually decreases; the third row says, “with the increase in topological charge m , the spiral extinction of the vector beam increases gradually, and the number is $2|m|$. The intensity distribution rotates counterclockwise with the polarizer, and the extinction is a left-handed spiral.” Figure 4c is the intensity distribution of a multimode vector beam when the polarizer is 45° . By observing the first row of the diagram, it can be seen that the shape of the Laguerre-Gaussian spot is changed into linear, triangular, quadrilateral, and pentagon spots, respectively. Figure 4d shows the intensity distribution of the multimode vector beam when the polarizer is 90° . It can be seen from the first row of the figure that when the topological charge m is constant, the number of extinction rings increases with the increase in n , and the number is $|n|$. In the second and third rows in Figure 4c,d, the same phenomenon occurs, as in the second and third rows in Figure 4b, the only difference is that they are equivalent to rotating 45° and 90° , respectively, on the basis of Figure 4b. Based on the above experimental results, it can be seen that the beam waist radius, topological charge number, polarization order, and additional phase of each beam can be independently controlled using this method. The first and second columns of the second row in Figure 3d–f correspond to the second and third rows of the first column of Figure 4b–d, respectively, and the image quality in Figure 4 is inferior to that of Figure 3. In other words, the light spots are more uniform and there is less noise in Figure 3. The fundamental reason is that the pixel size of the SLM is constant, and there are many types of vector beams generated in Figure 4, so the number of samples in Figure 4 is relatively small, which eventually leads to the fact that the more types of vector light fields there are, the worse the imaging quality.

4. Conclusions

In this paper, we propose an optical system that leverages the modified off-axis interference hologram coding method and the superposition principle in optics. This system is based on a transmission liquid crystal SLM combined with optical elements, including optical lenses. It has the capability of generating multi-mode vector light fields with complex amplitude distributions. As a proof of concept, we demonstrate the simultaneous generation of 12 vector beams with varying polarization distributions and spatial shapes on a single SLM. Importantly, this method is not limited to generating only 12 beams; it can generate an unlimited number of vector beams, primarily restricted by the resolution of the SLM. This innovative approach allows for the independent control of parameters such as the waist radius, topological charge number, polarization order, and additional

phase for each beam. Compared to existing methods, our system boasts a compact optical design, avoiding the need for complex optical components, while offering excellent programmability and flexible control. The potential applications are vast, from enhancing optical communication and optical interconnection to expanding the bandwidth of optical field channels. Furthermore, it holds promise in optical manufacturing and optical capture, making it a versatile and impactful technology in the realm of optics.

Author Contributions: Writing—original draft preparation, W.Z.; writing—review and editing, F.G., Q.F., X.Z., Y.X., B.Z. and S.K.; project administration and funding acquisition, Y.X. and F.G. All authors have read and agreed to the published version of the manuscript.

Funding: This research is supported by the National Natural Science Foundation of China (61905103, 61905136) and the Natural Science Foundation of Shandong Province (ZR2021QF025).

Institutional Review Board Statement: Not applicable.

Informed Consent Statement: Not applicable.

Data Availability Statement: The data presented in this study are available on request from the corresponding author. The data are not publicly available due to the data form part of an ongoing study.

Acknowledgments: S. Kumar acknowledges Double-Hundred Talent Plan of Shandong Province, China.

Conflicts of Interest: The authors declare no conflicts of interest.

References

1. Zhang, H.; Gao, K.; Han, L.; Liu, S.; Mei, T.; Xiao, F.; Zhao, J. Nanometric displacement sensor with a switchable measuring range using a cylindrical vector beam excited silicon nanoantenna. *Opt. Express* **2021**, *29*, 25109–25117. [[CrossRef](#)] [[PubMed](#)]
2. Rajesh, K.B.; Anbarasan, P.M. Generation of sub-wavelength and super-resolution longitudinally polarized non-diffraction beam using lens axicon. *Chin. Opt. Lett.* **2008**, *6*, 785–787. [[CrossRef](#)]
3. Gao, X.-Z.; Zhao, P.-C.; Sun, X.-F.; Yang, F.; Pan, Y.; Li, Y.; Tu, C.; Wang, H.-T. Highly purified transversely polarized optical needle generated by the hybridly polarized vector optical field with hyperbolic symmetry. *J. Opt.* **2020**, *22*, 105604. [[CrossRef](#)]
4. Sundaram, C.M.; Prabakaran, K.; Anbarasan, P.M.; Rajesh, K.B.; Musthafa, A.M. Creation of Super Long Transversely Polarized Optical Needle Using Azimuthally Polarized Multi Gaussian Beam. *Chin. Phys. Lett.* **2016**, *33*, 064203. [[CrossRef](#)]
5. Zhang, W.; Zhang, L.; Meng, C.; Gao, F. Generation of nanosecond cylindrical vector beams in two-mode fiber and its applications of stimulated Raman scattering. *Chin. Opt. Lett.* **2021**, *19*, 010603. [[CrossRef](#)]
6. Zhang, G.-B.; Gao, X.-Z.; Sun, X.-F.; Ma, R.; Wang, Y.; Pan, Y. Airy-Gaussian vector beam and its application in generating flexible optical chains. *Opt. Express* **2023**, *31*, 30319–30331. [[CrossRef](#)]
7. Zhu, L.; Deng, M.; Lu, B.; Guo, X.; Wang, A. Turbulence-resistant high-capacity free-space optical communications using OAM mode group multiplexing. *Opt. Express* **2023**, *31*, 14454–14463. [[CrossRef](#)]
8. Yang, B.; Chen, Y.; Wang, F.; Cai, Y. Trapping two types of Rayleigh particles simultaneously by a focused rotational elliptical Laguerre–Gaussian correlated Schell-model beam. *J. Quant. Spectrosc. Radiat. Transfer.* **2021**, *262*, 107518. [[CrossRef](#)]
9. Chen, K.; Li, Z.; Sun, X.; Kang, X.; Wang, G.; Gao, X. Free-space generation of three-dimensional tunable vector optical cages. *J. Opt. Soc. Am. A.* **2023**, *40*, 1809–1816. [[CrossRef](#)]
10. Xia, J.; Yang, Z.; Chen, H.; Du, Z.; Lü, Y. Tangentially and radially polarized Nd: YAG hollow lasers with two pairs of axicons. *Infrared Phys. Technol.* **2020**, *107*, 103301. [[CrossRef](#)]
11. Morohashi, T.; Srinivasa Rao, A.; Omatsu, T. Direct generation of lower-order cylindrical vector vortex modes from an end-pumped Pr³⁺: LiYF₄ laser. *Appl. Opt.* **2023**, *62*, 9183–9187. [[CrossRef](#)] [[PubMed](#)]
12. Otsuka, K.; Chu, S.-C. Microchip solid-state cylindrical vector lasers with orthogonally polarized dual laser-diode end pumping. *Opt Lett.* **2013**, *38*, 1434–1436. [[CrossRef](#)] [[PubMed](#)]
13. Ahmed, M.A.; Voss, A.; Vogel, M.M.; Graf, T. Multilayer polarizing grating mirror used for the generation of radial polarization in Yb: YAG thin-disk lasers. *Opt Lett.* **2007**, *32*, 3272–3274. [[CrossRef](#)] [[PubMed](#)]
14. Yang, H.; Xie, Z.; Li, G.; Ou, K.; Yu, F.; He, H.; Wang, H.; Yuan, X. All-dielectric metasurface for fully resolving arbitrary beams on a higher-order Poincaré sphere. *Photonics Res.* **2021**, *9*, 331–343. [[CrossRef](#)]
15. Wang, D.; Liu, F.; Liu, T.; Sun, S.; He, Q.; Zhou, L. Efficient generation of complex vectorial optical fields with metasurfaces. *Light Sci. Appl.* **2021**, *10*, 67. [[CrossRef](#)] [[PubMed](#)]
16. Hu, Y.; Ma, Z.; Zhao, W.; Zhao, J.; Liu, J.; Jing, Q.; Dou, J.; Li, B. Controlled generation of mode-switchable nanosecond pulsed vector vortex beams from a Q-switched fiber laser. *Opt. Express* **2022**, *30*, 33195–33207. [[CrossRef](#)] [[PubMed](#)]
17. Wang, S.; Xu, J.; Zhong, Y.; Ren, R.; Lu, Y.; Wan, H.; Wang, J.; Ding, J. Focus modulation of cylindrical vector beams through negative-index grating lenses. *Opt. Commun.* **2016**, *372*, 245–249. [[CrossRef](#)]

18. Liang, Y.; Yan, S.; Yao, B.; Lei, M.; Min, J.; Yu, X. Generation of cylindrical vector beams based on common-path interferometer with a vortex phase plate. *Opt. Eng.* **2016**, *55*, 046117. [[CrossRef](#)]
19. Geng, J.; Fang, X.; Zhang, L.; Yao, G.; Xu, L.; Liu, F.; Tang, W.; Shi, L.; Qiu, M. Controllable generation of large-scale highly regular gratings on Si films. *J. Light Adv. Manuf.* **2021**, *2*, 274–282. [[CrossRef](#)]
20. Zhang, Y.; Wen, S.; Wang, S.; Zhang, J.; Tang, C.; Zuo, H.; Gao, F.; Fan, F.; Zhang, Q.; Xu, Q. Fully continuous spiral phase plate for ultraintense optical vortices. *Opt. Lett.* **2023**, *48*, 2760–2763. [[CrossRef](#)]
21. Liu, X.; Zhou, J.; Xue, J.; Meng, Z. Coaxial multi-ring optical vortex generation based on compound spiral phase plates. *Laser Phys.* **2022**, *32*, 035402. [[CrossRef](#)]
22. Guo, L.; Feng, Z.; Fu, Y.; Min, C. Generation of vector beams array with a single spatial light modulator. *Opt. Commun.* **2021**, *490*, 126915. [[CrossRef](#)]
23. Qian, B.; Zeng, T.; Chen, Z.; Ding, J. Generation of vector beams using a Wollaston prism and a spatial light modulator. *Optik* **2017**, *148*, 312–318. [[CrossRef](#)]
24. Liu, S.; Qi, S.; Zhang, Y.; Li, P.; Wu, D.; Han, L.; Zhao, J. Highly efficient generation of arbitrary vector beams with tunable polarization, phase, and amplitude. *Photonics Res.* **2018**, *6*, 228–233. [[CrossRef](#)]
25. Rosales-Guzmán, C.; Bhebhe, N.; Forbes, A. Simultaneous generation of multiple vector beams on a single SLM. *Opt. Express* **2017**, *25*, 25697–25706. [[CrossRef](#)]
26. Kumar, P.; Pal, S.K.; Nishchal, N.K.; Senthilkumaran, P. Non-interferometric technique to realize vector beams embedded with polarization singularities. *J. Opt. Soc. Am. A* **2020**, *37*, 1043–1052. [[CrossRef](#)]

Disclaimer/Publisher’s Note: The statements, opinions and data contained in all publications are solely those of the individual author(s) and contributor(s) and not of MDPI and/or the editor(s). MDPI and/or the editor(s) disclaim responsibility for any injury to people or property resulting from any ideas, methods, instructions or products referred to in the content.